A solution to the hot cracking problem for aluminium alloys manufactured by laser beam melting

Mathieu Opprecht, Jean-Paul Garandet, Guilhem Roux, Camille Flament, Mathieu Soulier

A solution to the hot cracking problem for aluminium alloys manufactured by laser beam melting

Mathieu Opprecht, Jean-Paul Garandet, Guilhem Roux, Camille Flament, Mathieu Soulier

Mathieu OPPRECHT, LITEN, CEA Grenoble, France, mathieu.opprecht@cea.fr
Jean-Paul GARANDET, LITEN, CEA Grenoble, France, jean-paul.garandet@cea.fr
Guilhem ROUX, LITEN, CEA Grenoble, France, roux.guilhem@cea.fr
Camille FLAMENT, LITEN, CEA Grenoble, France, camille.flament@cea.fr
Mathieu SOULIER, LITEN, CEA Grenoble, France, mathieu.soulier@cea.fr

Corresponding author: mathieu.opprecht@cea.fr/ 04.38.78.47.69

Graphical abstract

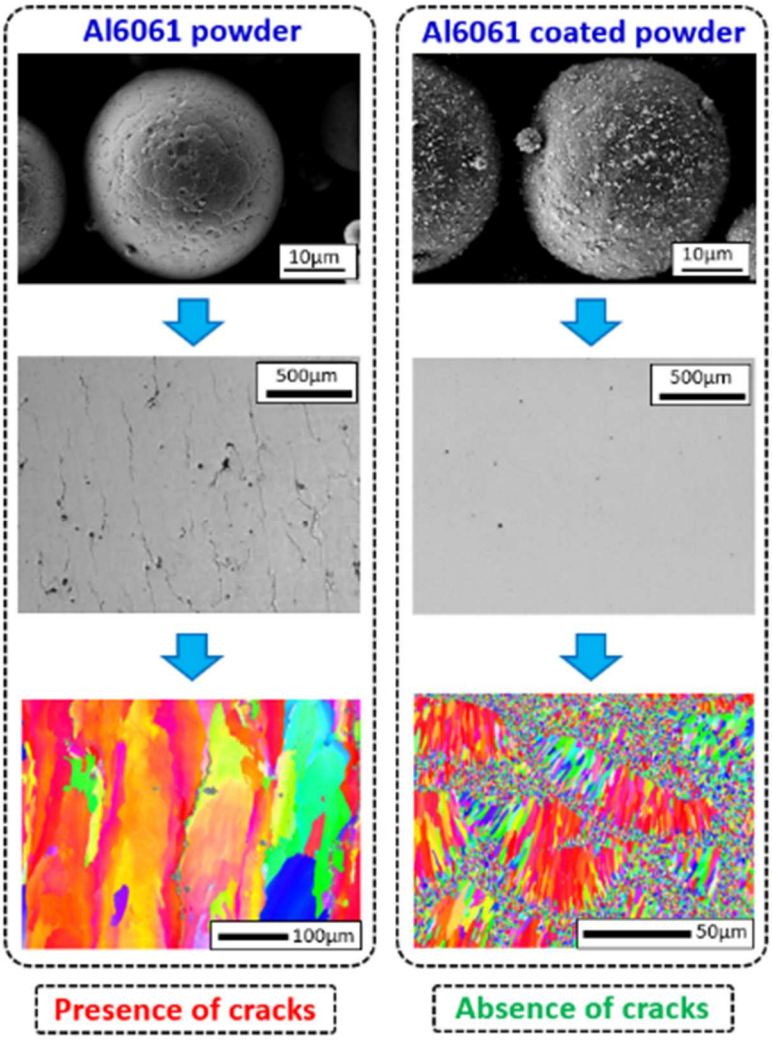

Keywords: Laser Beam Melting / Hot cracking / Aluminium Alloy / Rapid Solidification / Powder mixing.

Abstract

A method to eliminate hot cracking phenomena for aluminium alloys in Laser Beam Melting (LBM) is presented in this paper, focused here on the 6061 alloy. 6061 is a precipitation-hardened aluminium alloy, containing magnesium and silicon as its major alloying elements. This alloy, commonly used in the aeronautic and automotive industries, thanks to its excellent weight to strength ratio and high thermal conductivity, is particularly prone to hot cracking, in particular during LBM processing. The solution to remove cracks proposed in the present paper is to induce grain refinement to avoid the development of large columnar structures. To this end, various quantities of Yttrium Stabilized Zirconia (YSZ) are added to an Al6061 base powder using a dry mixing (Turbula®) procedure. Experiments highlight a grain refinement effect depending on the added YSZ quantity. From 1 vol% on, SEM and EBSD images reveal an equiaxed-columnar bimodal grain microstructure. Results show that the addition of 2 vol% YSZ allows to fully avoid cracks due to a continuous equiaxed band at melt pool boudaries. Additionally, TEM and DRX investigations provide new insights into the becoming of added particles along the printing process. The experimental results are then discussed on the basis of a number of existing solidification models, with a focus on the necessary conditions for the establishment of an equiaxed solidification regime.

1. Introduction

Laser beam melting (LBM), like most additive manufacturing (AM) processes is a layer-by-layer technique. Each powder layer is melted by a focused laser beam according to a desired geometry. The main potential for LBM is the ability to produce complex functional parts with, in most cases, no custom tooling. Additionally, powders can be recycled, which reduces waste.

In recent years, a lot of research has focused on the optimisation of the LBM process parameters in order to obtain dense parts with high mechanical properties. The range of materials that can be processed by this technique is still rather limited, the most relevant today being TA6V, 316L, Inconel 718 and AlSi10Mg [1]. Only a few Al-Si based cast alloys have been crack free processed [2],[3],[4],[5]. As for wrought Al alloys which are already known for their poor weldability, the application of LBM is considerably limited due to the presence of high thermal gradients that promote columnar growth and thus hot cracking. The level of cracking is particularly high during the LBM of Al6061 [6] and Al7075 [7].

Reasons for hot cracking are globally similar between the different solidification processes of welding and LBM. In both cases, process parameters induce thermomechanical stresses, which are a key ingredient to cracking. However, it appears unlikely that an easy solution can be found along this line in LBM, as thermomechanical stresses can not be controlled in industrial 3D practice. The drastic reduction in terms of thermal gradient that would be necessary to significantly reduce these stresses is hardly attainable by playing on LBM parameters or environment. Second, the alloying elements, selected to produce complex strengthening phases during additional heat treatment, often increase the solidification ranges, which is a

priori not favourable for crack sensitive alloys [8]. Last but not least, it is known that high thermal gradients encountered in 3D printing, generally induce a columnar microstructure, elongated in the building direction, which is known to promote hot cracking.

To reduce the sensitivity to hot cracking, it has been clearly demonstrated that fine equiaxed microstructures accommodate more easily strains [9]. In particular, equiaxed growth provide easier grain rotation and deformation during strain accommodation.

Two approaches enable grain refining. The first solution is to modify the thermal load during printing. At the process level, the key variables are the scanning speed, the heat source in terms of both intensity and spatial distribution, and in addition, wherever applicable, the build plate temperature [6]. From a more physical standpoint, the governing parameters are the solidification velocity and the temperature gradient. Along this line, microstructure changes can be obtained [10], [11]. A second way is to enhance heterogeneous nucleation, by changing alloy composition or by directly adding a nucleant agent in the base powder [12], [13], [14], [15], [16].

Recently, Montero Sistiaga et al. [17] demonstrated that the addition of 4wt% of pure silicon to Al7075 powder fully avoids cracking during LBM through a change of microstructure. Another success story in this microstructure control line was proposed by Martin et al. [16], by adding a nucleant agent to Al7075 powder, they successfully printed crack free parts. Other attempts have focused on developing new gas atomised alloys dedicated to LBM. The best known example is the Scalmalloy®, an Sc- and Zr-modified 5xxx alloy specifically developed by the Airbus APWorks© for the LBM process. The precipitation of Al_3Zr/Al_3Sc favourable nucleant phase is the main reason for the elimination of the hot cracking effect. Thereby, many studies focused on this

alloy [12], [14], [18], [19], [20], [21]. The Scalmalloy way is efficient but costly as it relies on the expensive Sc rare earth element.

The current work aims at the identification of the solidification control parameters as a way to remove cracks in crack sensitive aluminium alloys using a low cost particles electrostatic coating process to graft nanosize YSZ particles on aluminium powder. Yttrium Stabilized Zirconia (YSZ) powder was selected for its low price and availability due to large scale production, easy handling and the ability to precipitate the Al_3Zr phase. Al_3Zr is an aluminium nucleant phase well known from casting and welding for α_{Al} FCC, thanks to its small interatomic spacing misfit [22].

In the study, the grain refinement effect of the added YSZ quantity is investigated during processing of Al6061 alloy.

2. Experimental Section

From now, the following abbreviations are used to improve readability: P2% refers to the 2 volumic % of blended powder (YSZ + Al6061) and M2% refers to the 2 volumic % processed material.

2.1 Materials

Gas atomized Al6061 powder was acquired from TLS© Technik Bitterfeld. The particle size was in the range of 20-63 µm in volume (Figure 1), with a D_{10}, D_{50} and D_{90} respectively equal to 27µm, 41µm and 62µm.

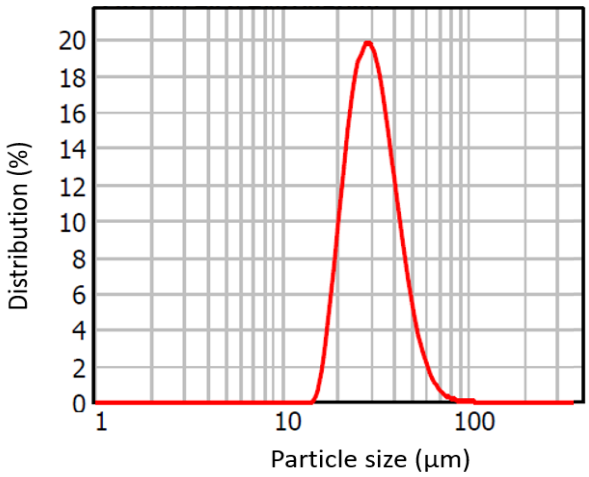

Figure 1 : Powder size distribution of Al6061 TLS powder.

Particles are globally spherical in shape (Figure 2), some of them with small satellites. Electron Backscatter Diffraction (EBSD) Inverse Pole Figure (IPF) map revealed an equiaxed microstructure with a typical grain size in the 5 µm range.

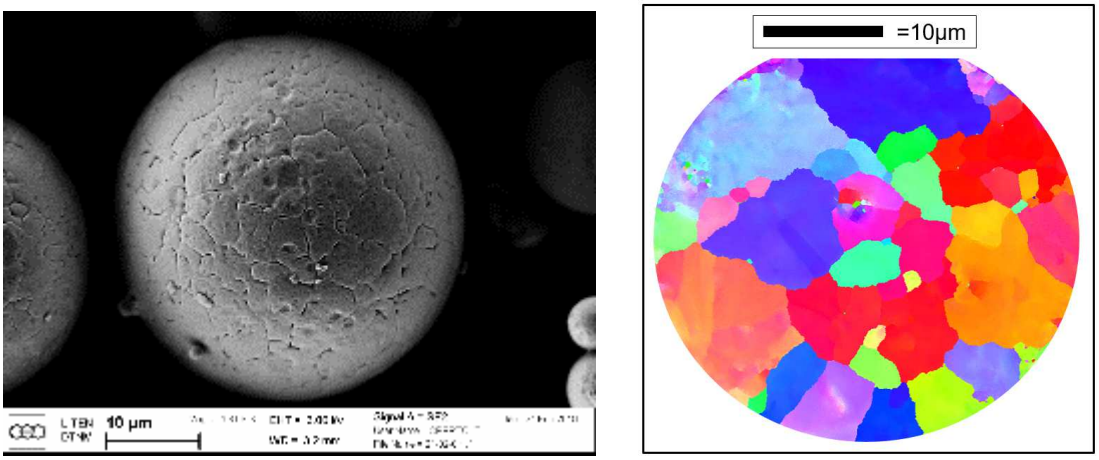

Figure 2 : left) Scanning Electron Microscopy image showing morphology of TLS Al6061 powder; right) EBSD IPF image of one TLS Al6061 particle.

The powder was dried at 150°C for 2 hours under vacuum prior to printing, in order to remove surface powder moisture that can lead to fine hydrogen porosity in final parts [5]. The chemical composition of the pre-alloyed powder used for LBM is shown in Table 1.

Al	Si	Mg	Fe	Cu	Cr	Ti	Mn
Bal	0.55	0.9	0.15	0.19	0.10	0.001	0.05

Table 1 : chemical composition of Al6061 powder (wt%).

Yttria-Stabilized Zirconia (YSZ) powder from INNOVNANO© was used, consisting of individual granules of about 60 nm size agglomerated in bundles of 240 nm in average, and a chemical composition detailed in Table 2.

ZrO_2	Y_2O_3	H_fO_2	Al_2O_3
94.3	3.6	1.7	0.4

Table 2 : Chemical composition of YSZ INNOVNANO © powder (wt%).

2.2 The mixing

The aim of this first step is to electrostatically make YSZ particles stick to aluminium powder, especially to avoid settling and to ensure a uniform distribution in the powder bed.

The mixing between Al6061 and YSZ powders was performed in a Turbula® set-up (T10B model) with a 6.5 liter volume mixing chamber. Blending is performed using 5mm diameter zirconia balls (roughly 200mL), and powders (1200mL of aluminium powder and 1-48mL of YSZ). Occupancy rate in the mixing box (volume ratio between powders/mixing balls and mixing box) is circa 20%.

From P0.05% to P2% YSZ addition, the mixing duration was 10 hours, and 20 hours for P4%. It was found that shorter mixing durations do not ensure a good YSZ particles grip on aluminium powder. To find the good mixing duration, optical granulometer was used (Malvern Morphologi G3S). Figure 3 represents granulometries of YSZ powder, Al6061 powder and P2% after one, three and ten hours of mixing. Peak associated to agglomerated YSZ particles (at roughly 0.6-1µm) decrease with mixing time, which trace YSZ particles gripping evolution on aluminium powders. For P2%, the granulometry after ten hours is close to that of the Al6061 powder, which indicates a

quasi-total coating of YSZ particles. For P4%, mixing time has been arbitrarily increased up to 20H.

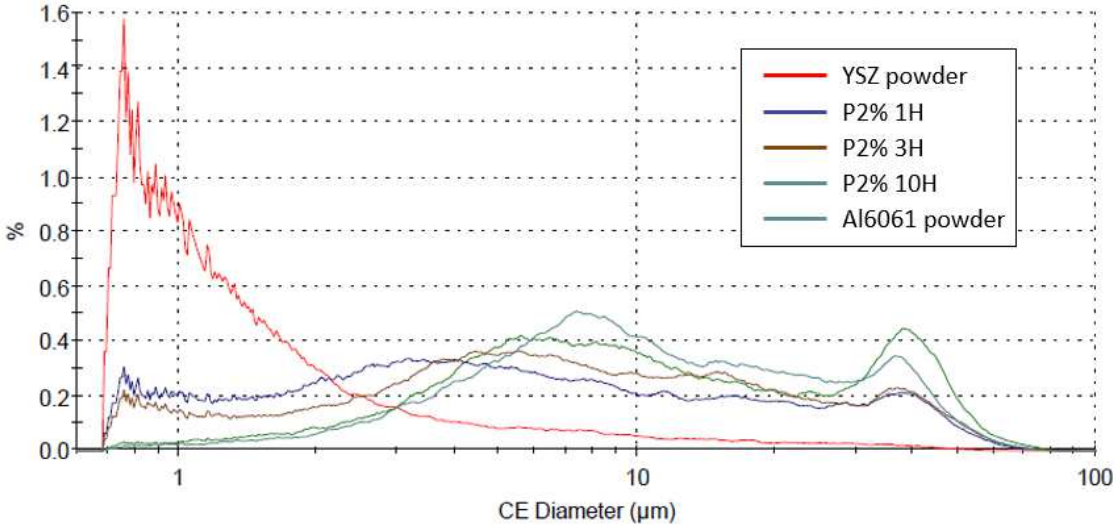

Figure 3 : Optical granulometries of YSZ powder, Al60061 powder and P2% after one, three and ten hours of mixing.

SEM images (Figure 4) revealed an overall uniform distribution of YSZ particles on the Al6061 powder. Even aluminium satellites seem to be well decorated with YSZ particles. For P4%, some YSZ bridges between Al6061 particles are observed.

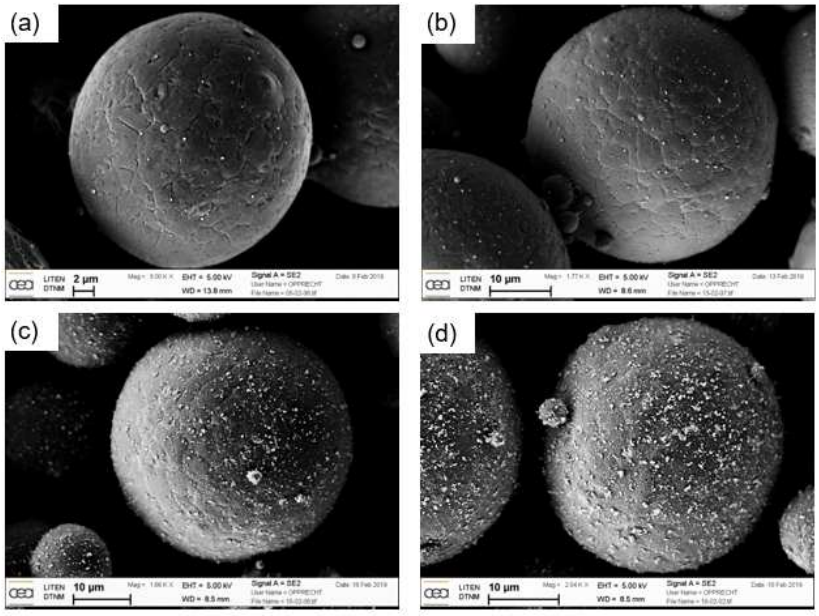

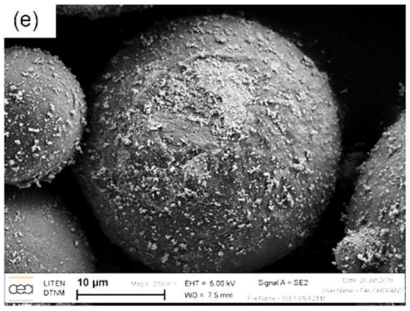

Figure 4 : SEM images showing (a) P0.05% ; (b) P0.2% ; (c) P1% ; (d) P2% ; (e) P4%.

It should be pointed out that similar type SEM images were observed on unmelted powders recovered after a 3D printing cycle. This result testifies of the good YSZ particles grip on aluminium powder and so of the robustness of this low cost mixing process.

To characterize the homogeneity in one mixing batch (P2%), four samples have been taken along the mixing box depth. Inductively Coupled Plasma (ICP) Optical Emission Spectroscopy (OES) measurements showed that overall, the homogeneity is good, with small deviations (Table 3).

	Al	Si	Mg	Zr	Y	O
Mean value between the four samplings (wt%)	95.46	1.06	0.82	1.14	0.05	0.18
Samplings standard deviation / Mean value (%)	0.32	1.11	1.31	2.61	2.43	13.42
Measurements standard deviation / Mean value (%)	0.13	0.92	0.61	0.31	1.82	5.71

Table 3 : ICP-OES measurements performed on P2%.

Especially, Zr quantity varies slightly between samples. It is worth mentioning that this variation is significant when comparing to the measurements standard deviation for one sample, which is much lower (0.3%), but that it nevertheless remains small enough

in terms of process control. In addition, the measured Zr value is consistent with the theoretical value based on a perfect sticking of the YSZ particles of 1.2wt% for P2%.

To conclude, this characterization supports the relatively good homogeneity of the mixing at the ICP measurement scale, which is of course much bigger than the melting pool one. Nevertheless, no significant signs of inhomogeneity have been pointed out after printing.

2.3 LBM process

Mixed powders were subjected to LBM manufacturing using two commercial machines: a 3D Systems PROX200, equipped with a 270W laser (spot diameter: 70µm), and a SLM Solutions SLM125, equipped with a 400W laser (spot diameter: 70µm). The two machines have a different layer spreading system: a counter rotating roll for the PROX200 and a polymer scraper for the SLM125. Cubic samples (10x10x10mm^3) were built with different laser powers and scanning speeds. Layer thickness and hatch distance were kept constant at 20µm and 100µm respectively, since the focus of the present work is mainly on microstructural issues and not so much on material quality aspects. Parts were built with a laser power varying from 150 W to 270 W (PROX200) / 400 W (SLM125) and a scan speed within the 300 mm/s to 1000 mm/s range. A scan strategy with parallel lines and no rotation between layers was applied for post characterization benefits. Printing is carried out in an inert argon gas atmosphere (O_2 content < 200 ppm) to minimize oxidation. The samples were grown on aluminium substrates (10x10 cm) that are not heated during the process. Densities were determined by the Archimedes method with an experimental standard deviation around 0.1% (five density measurements for each cube). For P2%, Figure 5 shows the

relationship between density and laser volumetric energy (LVE), defined as the laser power divided by the product of the laser speed and the spot area [23].

$$LVE = \frac{P_{laser}}{v_{laser} \times \pi \times r_{spot}^{2}} \quad (1)$$

At low volumetric energy and for a given hatch value, a poor densification is explained by a lack of fusion. At the other end of the energy range (>80 J/mm3), a good densification with a flat response to volumetric energy increases is observed on the PROX200 machine, the process seems to be quite robust. The situation is rather different on the SLM125 machine, where densification values appear scattered. A number of mechanisms (melt pool behaviour, more stable initial density of the powder bed with the roll spreading…) could be invoked to account for such a result, but no clear explanation can be given at this point. Nevertheless, this is not a problem for the present work, whose focus, as mentioned above, is mainly on microstructural issues and not so much on material quality aspects.

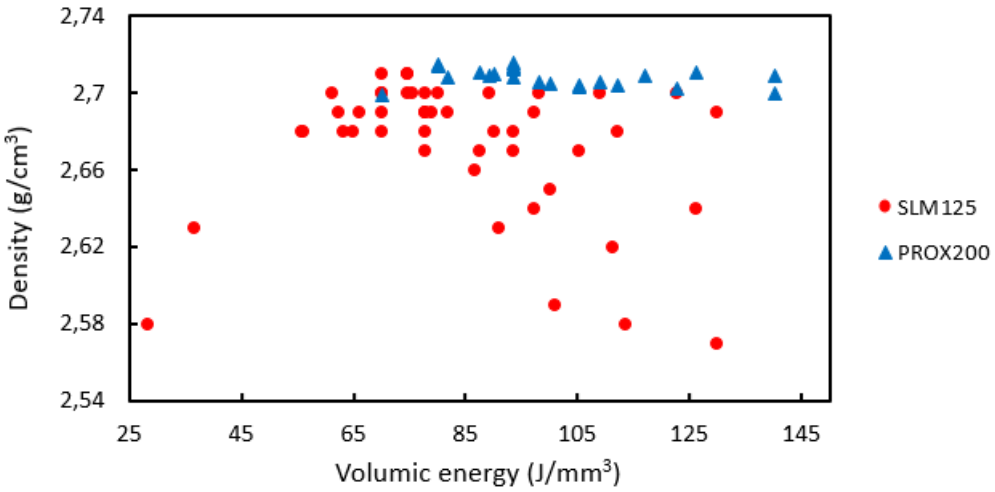

Figure 5 : Relationship between density (g/cm³) and volumetric energy (J/mm³).

For both machines, a maximum densification was found around 99%. ICP analysis (Table 4) on a 1 cm^3 M2% sample highlight an important Mg loss (which is consistent with its high partial pressure).

	Al	Si	Mg	Zr	O
Powder (wt%)	95.45	1.06	0.82	1.14	0.17
3D printed sample (wt%)	95.58	1.09	0.55	1.19	0.13
Deviation (%)	0.1	2.8	-49.4	4.2	-36.7

Table 4: ICP-OES measurements performed on M2% (1cm^3) and compared to the average values for the mixing.

Overall, the 3D printed sample features the same Zr concentration than that of the initial blend which brings additional support regarding the good grip of YSZ particles on aluminium powder. Thereby, YSZ particles are well integrated in the melt pool.

2.4 Characterization equipments

Optical microscopy was carried out with a DM 2500M (LEICA) at magnification 50x. X ray tomography was performed on a Phoenix Nanotom. Grains size, morphology and orientation were characterized by electron backscatter diffraction (EBSD) analyses on a LEO 1530 VP Gemini Field Effect Gun (FEG) SEM at 20kV equipped with a HKL detector. The surface of the samples was mirror polished thanks to a finishing step with 0.03 µm colloidal silica. The post processing was performed on CHANNEL 5 software (https://nano.oxinst.com/products/ebsd/post-processing-software), with grain boundaries defined for misorientation higher than 15°. A step size of 0.1 µm was used for high magnifications, and 0.3-0.4 µm for low magnifications. The crystal structure of the material was characterized by X-ray diffraction (Brücker D8 Advance). The measurements were carried out on the polished surfaces at ambient conditions using the θ–2θ technique with Cu Kα radiation.

Focused Ion Beam lift out method using a Thermo-Fisher Strata 400S FIB-SEM instrument was used to prepare TEM lamellas. It allows to locate material sampling in the area of interest, i.e. equiaxed or columnar regions for instance. Conventional and Scanning - Transmission electron microscopy (S-TEM) investigations were conducted with a Thermo-Fisher Osiris Tecnai instrument, equipped with a X-FEG source and operating at 200kV. STEM images were acquired on bright field (BF) and high angular annular dark field (HAADF) detectors. Energy dispersive X-ray spectroscopy (EDX) was conducted in STEM mode thanks to the Super-X EDX system with four Silicon Drift Detectors technology. EDX hypermaps were acquired with Esprit 1.9 software (Bruker). The crystallographic structure of precipitates was characterized thanks to high resolution TEM (HRTEM) using a 200 kV Thermo-Fisher Tecnai G2 FEG-TEM.

2.5 Cracks and grain size characterizations

Distances between cracks have been evaluated on the micrographs through a Matlab program based on image binarization. For each YSZ addition quantity, five images of size 2*1.5mm² were taken in the YZ plane from polished samples.

In addition, the total cracks length per unit of area (m/m²) has been evaluated on the same images from ImajeJ software. Each crack length was counted thanks to the image scale and summed to get the total cracks length per unit surface.

To calculate grain sizes, an elliptic fitting method was carried out on ImajeJ to get the length and width information. Starting from an EBSD image, a binarization is applied. Then ImajeJ fits the largest ellipse in each detected grain. All information is collected on Excel. Columnar grains are characterized by an aspect ratio (width/length) less than 0.5 with a length exceeding 3µm (that is twice that of the larger equiaxed grains). Such a procedure allows to separate equiaxed and columnar grains.

3. Results

3.1 XRD

Figure 6 shows the X-ray diffraction patterns measured on YSZ powder, Al6061 powder, P2%, M2% and M4%. For P2%, M2% and M4%, the (100), (200) and (220) main crystallographic orientations of alpha-aluminium phase (α_{Al}) are observed.

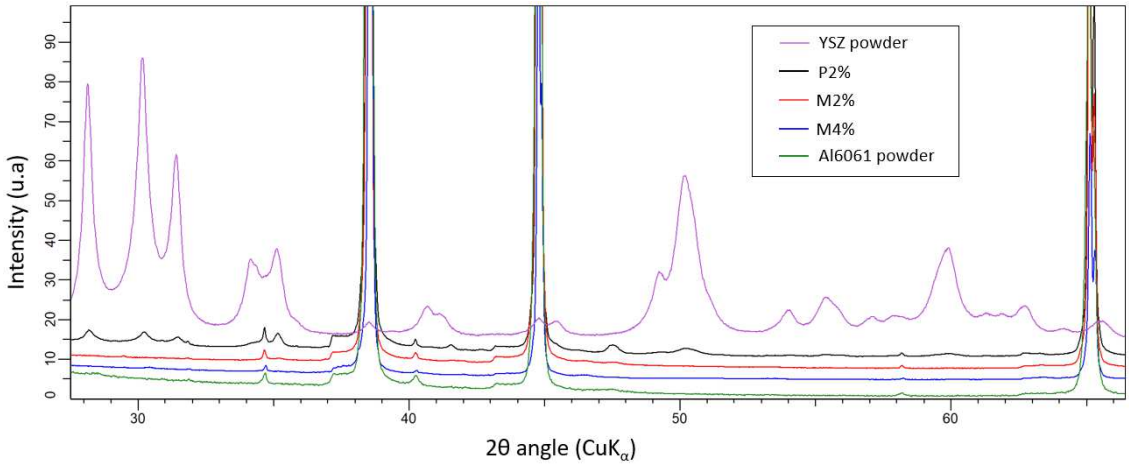

Figure 6 : Diffraction spectra for, from top to bottom: YSZ powder, P2%, M2%, M4%, Al6061 powder.

Regarding P2%, peaks related to YSZ powder and peaks associated to α_{Al} phase are present. Once mixtures are 3D printed, peaks related to YSZ powder are no more observed. This means that a large amount of YSZ particles have been melted, dissolved or have reacted. This result is in good accordance with the TEM EDX measurements that will be discussed in section 3.3.

3.2 Printing and optical micrographs

This section describes the influence of added YSZ quantity on crack susceptibility. For all characterizations, cubes with same laser power and scan speed (and therefore same volumetric energy) were selected. Micrographs (Figure 8) of unetched polished samples highlight the variation of crack quantity and length versus the added quantity of YSZ. From M0.05% to M1% samples exhibit a significant number of cracks, oriented parallel to the build direction (BD) (X being the laser axis progress, see Figure 7). For

both planes (YZ or perpendicular to BD XY), the number of cracks significantly decreases for M1%. For M2% no cracks are observed, as is also the case for M4%. Tomography on cubic samples, with a 6 µm resolution, confirmed the absence of cracks.

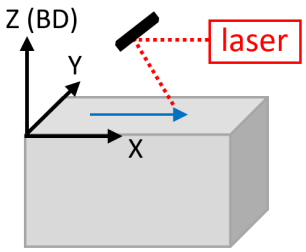

Figure 7 : diagram of LBM process with the axis and the scanning direction (X).

For all printed batches, a few spherical defects ranging from 1 to 50 µm are found. They are mainly attributed to occluded gases. Indeed, many researches have reported spherical gas porosity occurring during aluminium alloys processing often attributed to hydrogen [24]. Solutions from casting and welding are hardly transferable to the LBM process [25], [26]. Nevertheless, Weingarten et al. [5] proposed a way to circumvent the problem. They showed that external powder drying, internal laser drying and scan speed adjustment can lead to a hydrogen pore density decrease.

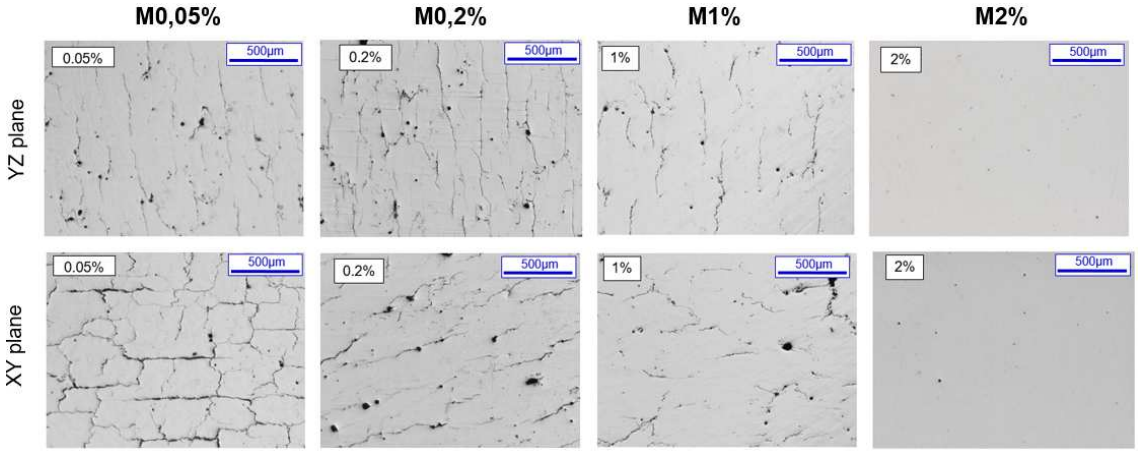

Figure 8 : Optical micrographs showing the evolution of hot cracking sensitivity with YSZ addition in YZ plane and perpendicular to BD, XY plane.

Regarding M2%, it is worth mentioning that even with set of parameters out of optimal range, no cracks are observed. Such a finding supported the fact that porosity

does not induce cracks. This approach thus appears to be process parameters independent in the range allowing densification level >90%, which is not always the case in Al-alloy sensitive to hot cracking [27]. Also, crack-free parts have been successfully built on both machines, which indicate that this approach is also machine independent. Last, these findings (complete absence of cracks) were supported by some supplementary mechanical tests that showed the as-built properties to be better compared to those of materials elaborated through conventional manufacturing routes.

Figure 9 shows the average value of mean cracks distance according to YSZ quantity, with errors bars representing standard deviation between the five samples.

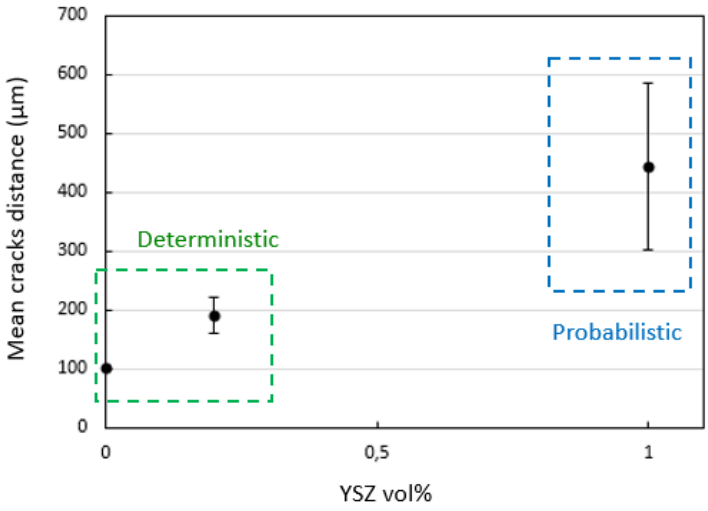

Figure 9 : Mean cracks distance versus YSZ quantity of addition (YZ plane).

Up to M0.2%, the standard deviation is quite small. The situation could be qualified as deterministic: cracks are regularly distributed. For no YSZ addition, the distance between cracks is close to the hatch distance (100µm). Above M0.2% of YSZ addition, the mean distance between cracks is twice larger, which is a first indication of YSZ influence on microstructure. For M1%, the distance between cracks varies from 300µm to 600µm. The cracks repartition is more probabilistic with larger deviations on

measured values. In any event, the distance between cracks globally increase with YSZ addition.

Figure 10 shows the average specific cracks length and the standard deviation over 5 images. Results show a sharp decrease between M0% and M0.2% and a somewhat linear variation up to M2%, where no more cracks were found.

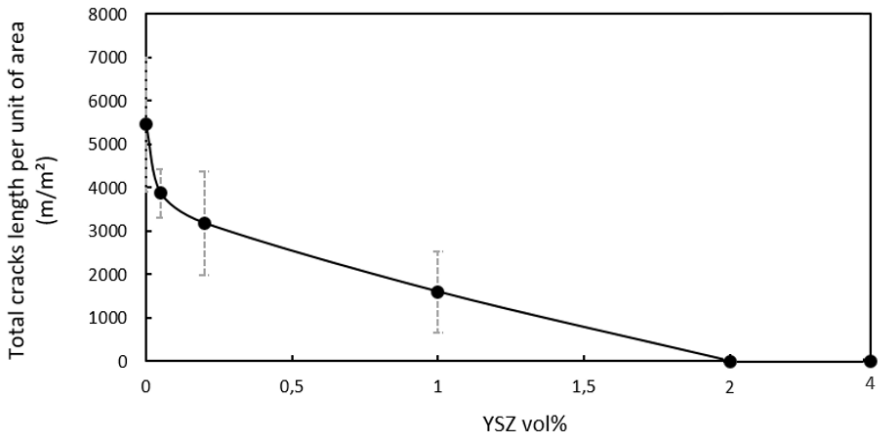

Figure 10 : Total cracks length per unit of area versus YSZ quantity of addition (YZ plane).

From these two results (decrease of total cracks length and increase of distance between cracks), it can be conclude that YSZ addition enables to decrease hot cracking sensitivity and to completely remove cracks for M2% and M4%.

3.3 Microstructure

Figure 11 presents EBSD images with grain boundaries marked by bold lines. Grey levels are displayed to correctly discern grains. For M0.05% and M0.2%, the large columnar grains oriented along the building direction must have been formed by epitaxial grain growth through two or more successive laser passes and cross multiple build layers. As shown in Figure 11, for M1% and M2%, an equiaxed-columnar bimodal grain structure is observed. For M2%, a fine equiaxed dendritic microstructure

continuously decorates each melt pool border (Figure 13). Inside the melt pool, coarser columnar grains are observed.

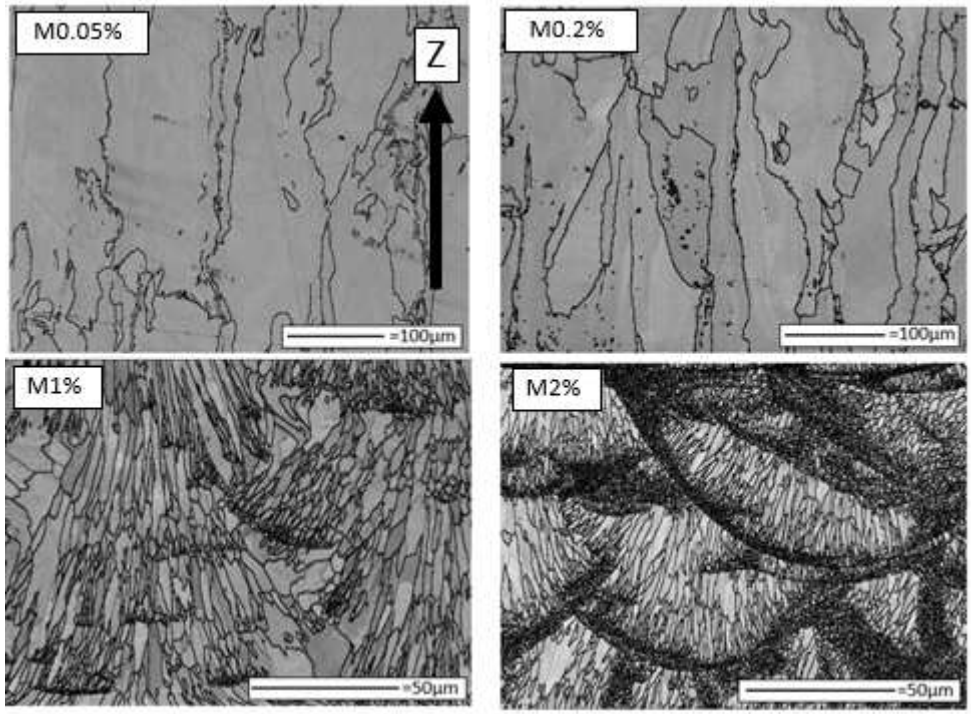

Figure 11 : EBSD images (grey levels + bold lines for grain boundaries) exhibit microstructures according to volumetric quantity of YSZ added.

Columnar grains size is divided by more than one order of magnitude from M0% to M2% (Figure 12). Equiaxed grains size is constant whatever the YSZ concentration. There are not so much differences in columnar grain sizes between M1% and M2%, and yet cracks are present in M1%, meaning that the size criterion is not sufficient by itself to discriminate the cracking behaviour.

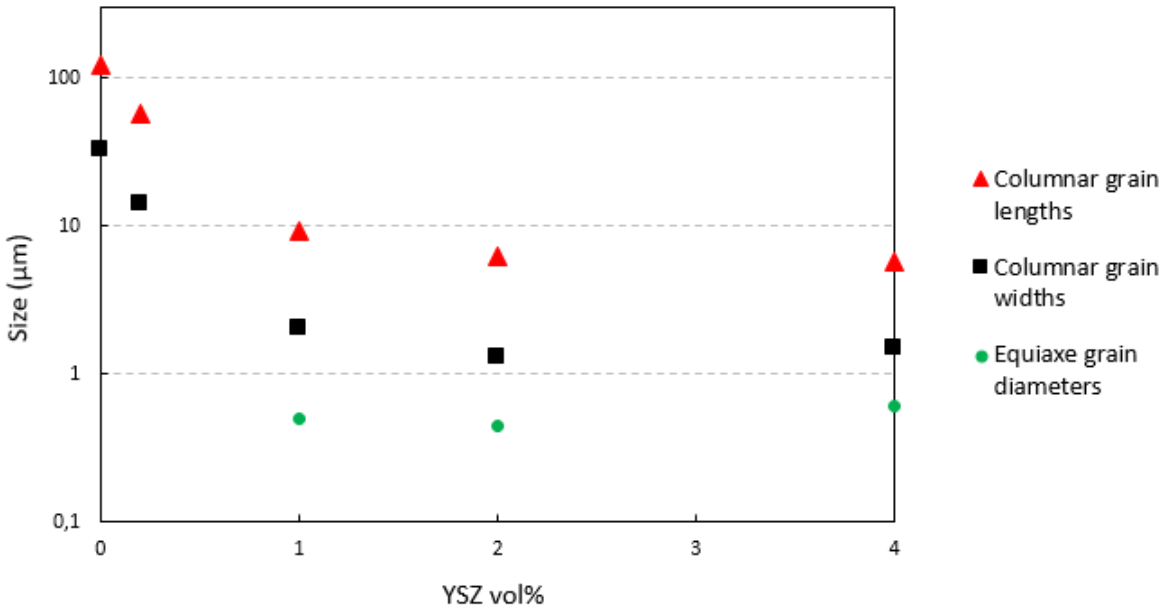

Figure 12 : Grain size versus volumetric quantity of YSZ added (for columnar grains both length and width values are plotted, for equiaxed grains the diameter as arithmetic mean of length and width is plotted).

Between M2% and M4%, a plateau is reached for all grain sizes. However, equiaxed grain fraction is increasing between 8% (2D measurement from EBSD image) for M1% to 63% (2D measurement from EBSD image) for M4%. From 1% on, columnar grains are quite short, which is likely due to the interruption of the columnar growth by refined equiaxed melt pool boundaries.

3.4 Focus on M2%

The 2 vol% concentration is interesting insofar as it is the lowest addition at which crack free growth can be achieved. EBSD Inverse Pole Figures have been recorded at various magnifications (IPF-Z Figure 13). A significant texture according to <100> direction is detected in the columnar regions. In contrast, in equiaxed grain zones, there is no evidence of any texture.

At low magnification, a lot of melting pools are visible. Two interesting observations can be pointed out. First, only melting pools with “large” columnar grains are textured, particularly the grains in the center (those aligned with BD). On the x750 EBSD map,

one can distinctly see that edges of melting pools are not textured, where growth orientation is mainly following the thermal gradient. Second, no significant large scale inhomogeneity is visible, which can be considered as a good indicator for the composite powder preparation process.

At high magnification, an interruption of columnar growth by a large equiaxed band at the bottom melting pool is clearly apparent. These equiaxed structures require fairly large amounts of undercooling for the nucleation step, which is far from obvious in AM processes. Specific sources of such undercooling are discussed in section 4.

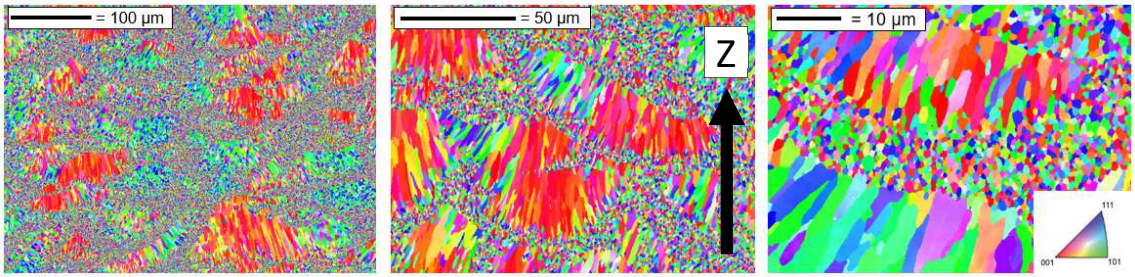

Figure 13 : EBSD IPF-Z at three different magnifications left) x250; center) x750 and right) x2000

An EDS (Energy Dispersive X-ray Spectroscopy) map in the equiaxed grain region was performed at 4keV (Figure 14), which corresponds to a 110 nm interaction pear (calculated on Casino [28] software). The first interesting point to mention is the aluminium impoverishment close to grain boundaries. Then, the concentration of alloying elements is higher along grain boundaries, meaning that the elements are likely to be rejected by diffusion at the solid/liquid interface. These results are consistent with the attainment of local thermodynamic equilibrium conditions at the interface.

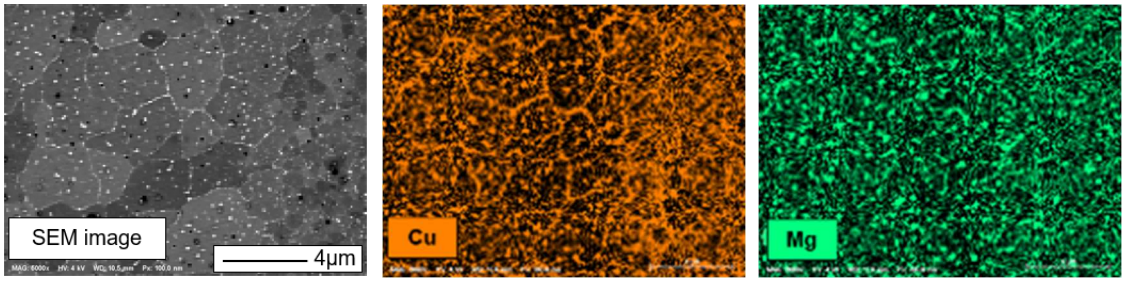

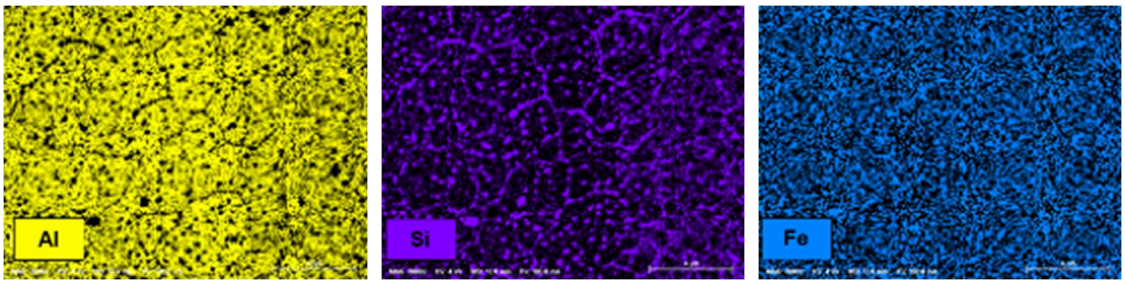

Figure 14 : EDS mapping of M2% showing Al, Cu, Mg, Si and Fe elements in an equiaxed zone.

STEM EDS measurements taken in the columnar grains region show Fe precipitates surrounded by Si/Mg precipitates (Figure 15). For this alloy, it is known from the literature that Mg-Si phases often precipitate on dispersoïds during thermal treatment at to the homogenization temperature [29]. These dispersoïds act as heterogeneous nucleation sites for the precipitation of coarse Mg-Si phases. No Zr precipitate was detected. However, this element appears in solid solution. A few oxides (Fe-oxides, Si-oxides, Mg-oxides) are present. Some of them are located along grain boundaries.

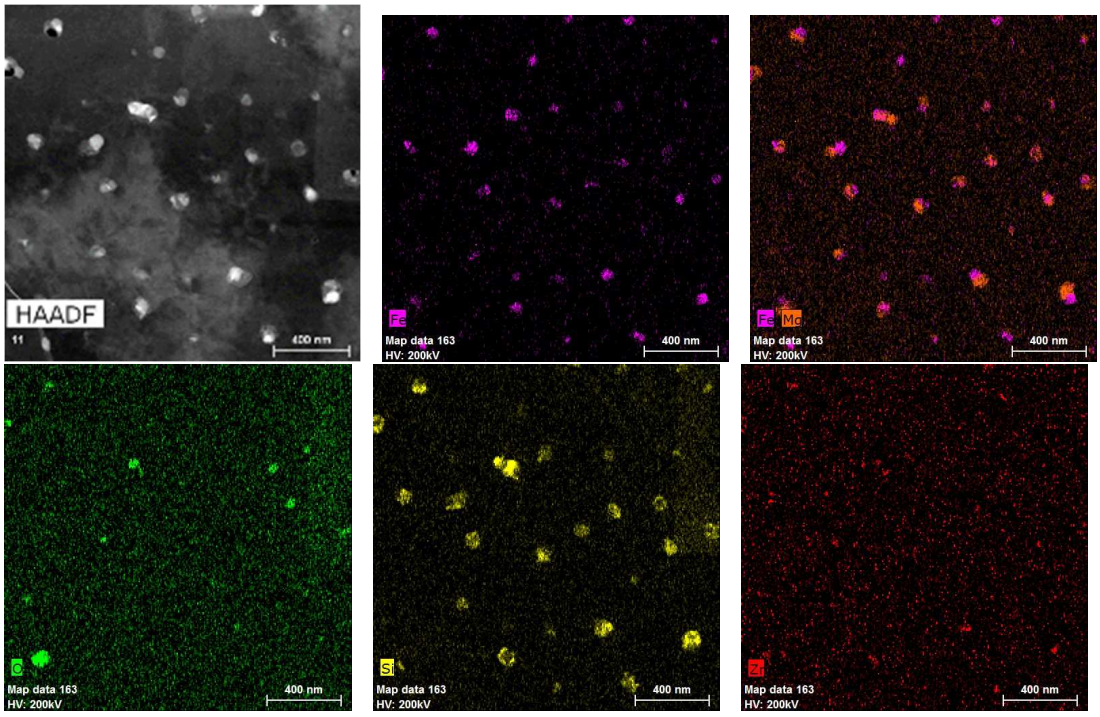

Figure 15 : STEM-EDX maps of the precipitates present inside a columnar grain showing Fe, Mg, O, Si and Zr elements.

As shown by SEM and TEM images, these precipitates are uniformly incorporated into the microstructure, which should bring additional strengthening (Figure 15). In the

same way, intra and intergranular precipitates are detected in equiaxed regions (Figure 16).

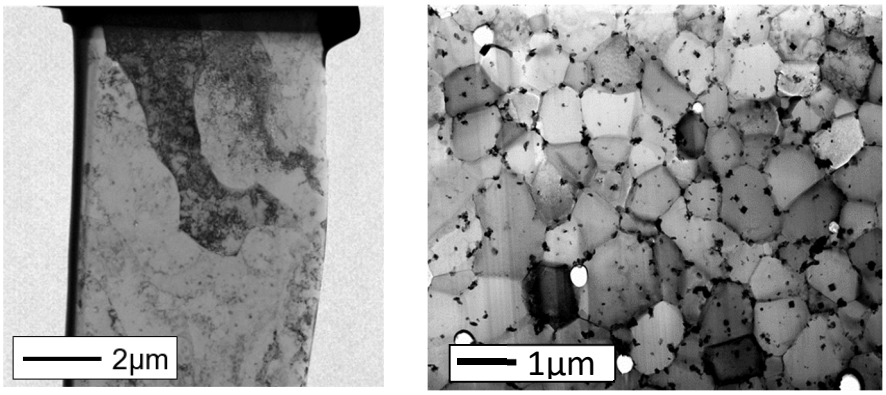

Figure 16 : BF-TEM images in a columnar region (left) and in an equiaxed region (right).

Unlike what is observed in columnar regions, Zr precipitates are present in the equiaxed regions, both along grain boundaries and interestingly inside grains. The number of intra-grain precipitates significantly varies from one grain to another. One possible explanation is that TEM observations are 2D projection of a 3D volume. Some precipitates, especially those inside grains, have cubic shapes, with a side length of approximately 100nm and enriched in zirconium. What is particularly relevant is the vicinity between these cubic shape Zr precipitates and small Mg/Al-oxide precipitates (Figure 17). It is worth mentioning that this link between oxides and Zr precipitates has been observed for three other selected grains. Other precipitates, like Si/Fe and Mg oxides, are detected mainly along grain boundaries.

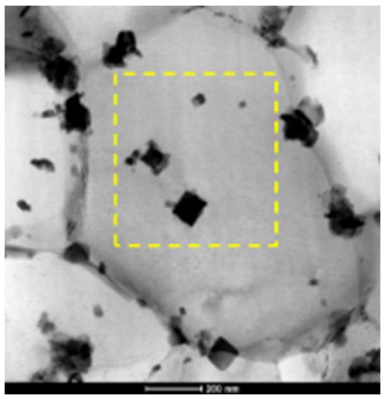

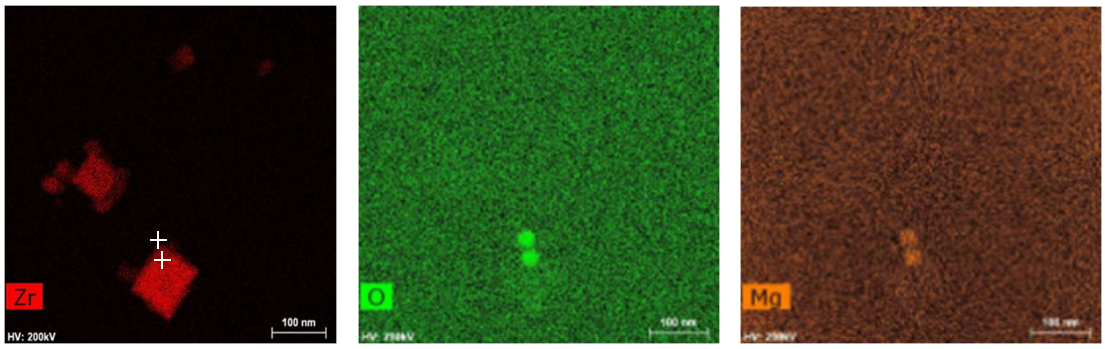

Figure 17 : BF-TEM image of one equiaxed grain with Zr, O and Mg EDX analysis in the yellow zone (dashed line). White crosses on Zr map locate the small Mg-oxides.

The crystallographic structure of Zr precipitates was investigated by selected area electron diffraction (SAED). Figure 18 shows SAED patterns of the Al matrix in [100] direction (left), of the biggest Zr precipitate of Figure 17 in Al matrix in [100] direction (center), and of another Zr precipitate in $[1\bar{1}4]$ direction. The diffraction spots associated to the Zr precipitate are circled in yellow on the SAED pattern. Diffraction patterns on several Zr cubic precipitates revealed a $L1_2$ faced centred cubic structure (FCC) with a lattice parameter close to twice the one of the aluminium matrix. Interestingly, the obtained value is also close to the lattice parameter of $MgAl_2O_4$ phase [12], which support the nucleation of Al_3Zr precipitate on such Mg/Al-oxides. Moreover an orientation relationship (OR) between the precipitate and the matrix is observed since $[100]_{Al}$ // $[100]_p$. This OR was also emphasized from the study of another grain oriented along $[1\bar{1}4]$ direction. As observed and as it is known from literature [30], this metastable structure of Al_3Zr phase is coherent with the matrix. The Fast Fourier Transformation (FFT) pattern associated to the matrix in green and the precipitate in blue further confirmed the expected $L1_2$ Al_3Zr structure and exhibited a high coherency (Figure 19.d).

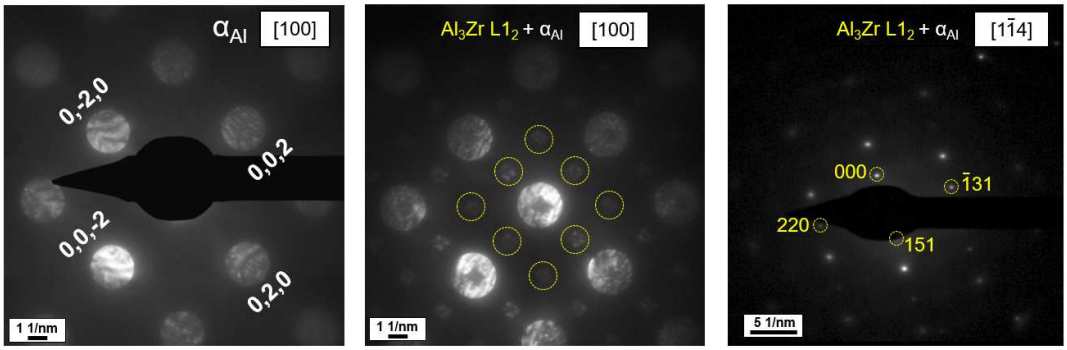

Figure 18 : Diffraction pattern of the matrix, and diffraction pattern of a $L1_2$ Al_3Zr precipitate in [100] direction and [1$\bar{1}$4] direction.

Figure 19.b/d shows HRTEM images of the Zr precipitate (surrounded in red on Figure 19.b) embedded in Al matrix. They confirm that the lattice parameter of Al_3Zr precipitate is twice the one of aluminium matrix ($d(0,0,2)_{Zr}$ = 0.40 nm ≈ 2 x $d(0,0,2)_{Al}$). The junction between both lattices in Figure 19.d is periodic and coherent.

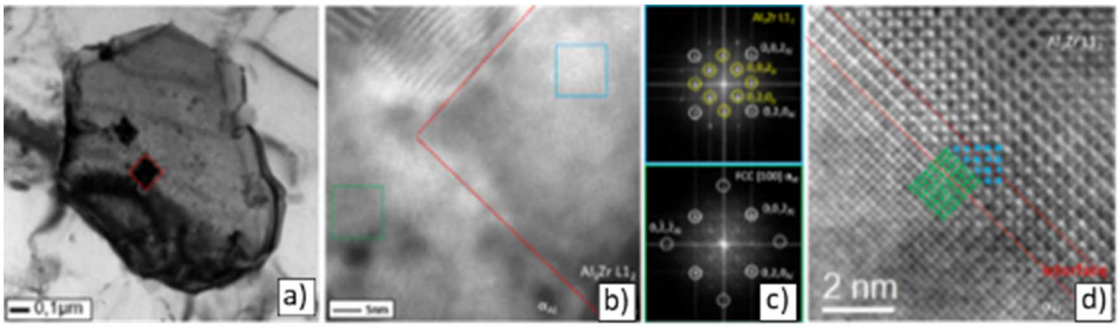

Figure 19 : HRTEM observation of Al matrix (green) / Al_3Zr precipitate (blue). (a) at low magnification (b) at higher magnification showing the interface (red) and (c) associated Fast Fourier Transformation (FFT). (d) HRTEM image at higher magnification.

It should be noted that for both columnar and equiaxed regions, no YSZ phases is detected by TEM, which is consistent with the absence of YSZ peaks in the XRD spectra of section 3.1.

4. Discussion

The objective in this section is to propose plausible scenarios, based on existing solidification models to account for the observed experimental results. The columnar

to equiaxed transition has been widely studied in foundry configurations. Hunt et al. [10] took into account nucleant density and chemical undercooling to derive a criterion for the transition in a thermal gradient and solidification speed plane. Later on, Greer et al [31] added the effect of capillarity undercooling. Nevertheless, the range of parameters studied cannot cover the LBM conditions. For instance, solidification velocities and temperature gradients are order of magnitudes higher, meaning that the models will have to be carried out far beyond their ascertained range. However, most of the relevant physico-chemical mechanisms involved are expected to remain valid, so that the existing models can be used, at least to provide a qualitative understanding.

It should also be mentioned that a number of numerical simulation studies focused on the transport phenomena within an additive fabrication melt (see e.g. for the case of Al based alloys ([12],[32],[31]). Close to this present focus is the very thorough recent work by Shi et al. [11] that went into the details of the solidification process, using in particular cellular automaton techniques to predict microstructures. But even though many interesting results have been obtained, the number of necessary assumptions remains quite high. Here the approach is more qualitative, based on order of magnitude arguments, but it allows to propose simplified explanation of what happens within the melt and in the vicinity of the growth front, in particular to rule out potential mechanisms.

The first thing that can be stated on the basis of Hunt's model [10] is that due to the extremely high temperature gradients (say of the order of 10^5-10^6 K/m) at the solid liquid interface, columnar growth is to be expected unless a sufficiently high number of efficient external seed particles are available. Figure 20 illustrates this possible extrapolation, at this point without questioning the Hunt's assumptions. The red star represent standard process values encountered in LBM ([32],[33]). Again, Hunt's

model has to be extended far away from its range of validity, but the present conclusion is drawn with a safety margin of a few order of magnitudes with respect to the theoretical predictions. Without a large number of external nucleation sites, the thermal gradient would have to be dramatically reduced, meaning order of magnitudes, e.g. through the use of an adapted heat source distribution [11] or heating plate in LBM conditions, to cross the columnar to equiaxed transition.

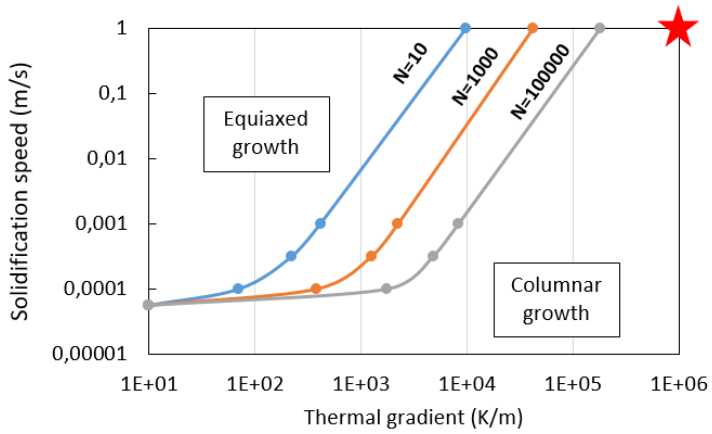

Figure 20 : Solidification speed versus thermal gradient for an Al-3wt%Cu alloy (extracted from figure 5 [10]) where N is the number of nucleation sites (in cm^{-3}) extended to solidification speed and thermal gradients encountered in LBM process (red star).

To go a step further, heterogeneous nucleation requires both the presence of efficient seeding particles in the vicinity of the growth front, and the existence of a supercooled zone ahead of the interface. Those two points should be adressed, as well as the question of the resumption of columnar growth as solidification proceeds.

4.1 Becoming of the added particles

To start with, it should be recalled that both DRX and TEM results highlight no evidence of remaining YSZ particles, neither in the equiaxed nor in the columnar region. Of course this limited sampling does not allow for an absolute conclusion to be drawn, but it can be safely stated that most YSZ particles do not survive the process.

A first question to be addressed is the possible melting of these particles. The maximum temperature within the melt pool is difficult to estimate, and is possibly extremely high in the vicinity of the laser area [12], but it can probably be stated that all the particles do not see a temperature of 2700°C (YSZ melting point). YSZ particles melting point has to be appreciated with regards to the Gibbs Thomson effect, which predicts that the effect of particle size is only significant below 40-50nm ([34], [35]). Thus, the 60 nm YSZ particles can be taken to have a melting temperature similar to the bulk material.

On the other hand, one could consider a surface reaction on the added nanoparticles, which could lead to the formation of the Al_3Zr precipitates detected in equiaxed zones. One should thus consider the reaction of zirconia with liquid aluminium according to:

$$3\ ZrO_2 + 13Al \rightarrow 3\ Al_3Zr + 2\ Al_2O_3 \quad \text{(i)}$$

However, the first point to be stated is that no evidence of any ZrO_2/Al_3Zr core shell structures that would support this surface reaction mechanism has been observed. Also, the size of observed Al_3Zr precipitates (≈100nm) do not well fit with primal YSZ particles.

The last possibility is that the YSZ or Al_3Zr (originated from (i)) particles simply dissolve in the melt, with a subsequent recombination of the liberated Zr with Al upon cooling according to the reaction:

$$3\ Al + Zr \rightarrow Al_3Zr \quad \text{(ii)}$$

Nevertheless, an important question regarding the nucleation kinetics mode remain. Indeed, the homogeneous nucleation rate is proportional to $\exp(-\frac{\Delta G*}{kT})$ where ΔG* represents the nucleation barrier at a given undercooling [35]. Taking reasonable values for the enthalpy of fusion of Al_3Zr, ΔH=305J/g [36], and the solid liquid interface

σ_{SL} = 1 Jm^{-2} , the nucleation barrier at 950 K (i.e. close to the growth temperature of the α_{Al} phase) is roughly $\Delta G^*=1.9x10^{-16}J$. Normalizing by kT, $\Delta G^*/kT$ is of circa 10^4. Even taking into account the very large 10^{40} ($Jm^{-3}s^{-1}$) prefactors of homogeneous nucleation, the number of stable clusters formed would be too low in practice.

Since homogeneous nucleation of the Al_3Zr is kinetically not favoured, it is proposed that Al_3Zr heterogeneously nucleates on oxides, mainly Al/Mg-oxides as TEM results pointed out. Among the constituents of the melt, Mg is by far the best reducer. This means that it will be able to capture oxygen, be it free oxygen coming from the dissolution of YSZ, or oxygen associated with either zirconium or aluminium. As the lattice spacing of $MgAl_2O_4$ [37] is very close to that of the measured Al_3Zr one (0.81nm), one may assume that the nucleation barrier will be very low, and that heterogeneous nucleation of Al_3Zr can take place on Al/Mg based oxides.

To conclude, YSZ particles probably dissolved in the melt. Subsequently some of the liberated/available oxygen reacts with Mg/Al and some of the Zr with Al to provide the $MgAl_2O_4$-Al_3Zr composite as seeds for the equiaxed growth of the α_{Al} phase.

4.2 Undercooled zone

The second requirement for equiaxed growth is the need of a supercooled zone of sufficient magnitude (in terms of temperature range) and dimension (in terms of spatial extent) ahead of the solid liquid front. In this section the three classical sources of interface undercooling are discussed.

The first contribution that comes to mind is the chemical one, since it is often dominant in welding/casting conditions. The extent of the undercooled zone, which depends on the state of convective-diffusive species transport in the melt, should be considered. To get an upper bound value of the thickness of this undercooled zone, let

us consider that mass transport proceeds mainly by atomic diffusion. In that case, it is known from the literature [38] that there will be a solute rich region ahead of the growth front, the extent of this boundary layer being at the most given as (2):

$$\delta_C = \frac{D_s}{v_i} \quad (2)$$

With D_s the solute diffusion coefficient in liquid and v_i the liquid/solid interface velocity. Taking an upper bound estimate for D_l ($10^{-8} m^2 s^{-1}$, [39]), a value of v_i in the m/s range will yield a boundary layer thickness of only 10nm. This result, in addition to the fact that the above value may be an overestimate (at melt velocities in the m/s range, it is far from obvious to a priori neglect convective solute transport), clearly rules out the chemical contribution to the necessary undercooling.

Another potential source of undercooling that can be safely ruled out is capillary undercooling. Indeed the observed columnar grains have dimensions in the µm range, in which the Gibbs Thomson effect can be safely neglected (see above). This lefts us with kinetic undercooling as the only remaining source.

This contribution is generally ignored in classical solidification processes, where growing interface speed is order of magnitudes lower than in LBM. In a dedicated study, G.H. Rodway and J.D. Hunt experimentally investigate this contribution for a lead specimen [40]. In the limited velocity range investigated (v_i < 10 mm/s), the undercooling remains below 0.1 K. By extending the observed linear relationship between freezing interface undercooling and velocity (figure 3 of [40]), a 4K kinetic undercooling is expected from a 1m/s interface velocity.

A second interesting paper to mention on this topic focuses on gallium interfaces growth kinetics. Considering the continuous growth model developed by Wilson [41] and Frenkel [42], which assumes an ideally rough interface so that all interfacial sites

are equivalent and probable growth sites, it is possible to calculate the growth undercooling contribution. After different considerations, Peteves et al. [43] have deducted a linear growth law for continuous kinetics undercooling (3):

$$v_i = K_C \times \Delta T \ (3)$$

With K_C a kinetic coefficient (order of some centimetres per second per K for most metals). Taking K_C = 3-4 $cms^{-1}K^{-1}$ and a solidification velocity of 1 m/s, this would amount to an undercooling value of 25-35 K.

Also to be mentioned in this respect is the work of W. Tan [44], that uses a numerical simulation to follow the growth of a dendrite and propose an empirical velocity undercooling kinetic. Their work pertains to austenitic stainless steel, but is more relevant in terms of solidification velocities. With a limited extrapolation, an undercooling of circa 40 K is expected at a solidification velocity of 1 m/s.

The experimental conditions being different than those of the literature, both in terms of materials and process parameters, the actual kinetic undercooling at the growth front is hardly calculable. Nevertheless, it appears reasonable to expect interface undercoolings ranging from a few K to a few tens of K, which, associated with a thermal gradient of 10^6K/m, would induce a kinetically undercooled zone of some micrometers or some tens of micrometers ahead the solidification front, sufficient to provide conditions allowing equiaxed growth.

4.3 Resumption of columnar growth

In all cases, equiaxed growth stops before the end of the process, and at some point columnar growth resumes. The first question that can be addressed regards how this happens. Some interesting insights can be gained on the basis of the obtained EBSD data. Among the various equiaxed grains, there are statistically some with an (100)

plane oriented normal to the thermal gradient, that will naturally grow columnar provided they are not hampered by any equiaxed shield. This leads us to the second and more intricate question, namely as to why columnar growth prevails in the melt pool.

To this end, it should be recalled that a transition in terms of nucleation sites density clearly appeared between equiaxed and columnar zones. Columnar zones are devoid of any Zr precipitate, which is by the way consistent with such kind of microstructure. As mentioned above, Al_3Zr nucleation on Al/Mg-oxides is responsible for the equiaxed growth. In columnar parts, these same oxides are present and nevertheless no Al_3Zr precipitate has been detected. Now, the question that needs to be addressed regard this nucleation sites density variation with melting pool depth.

One may first wonder about the homogeneity of the Zr concentration within the melt, in relation to convective mixing. To do so, one can to the first order derive a chemical transport Peclet number defined as (4):

$$Pe = \frac{v_{convection} \times melting\ pool\ depth}{D_s} \quad (4)$$

Taking an upper bond solute diffusion coefficient in liquid of $10^{-8} m^2/s$ [39] and a reasonable value of the fluid velocity (driven to the first order by Marangoni convection) of 1 m/s, a melting pool depth of 100 µm leads to a Pe number of 10^4. It can thus be stated that the available Zr should be homogeneously distributed.

However, the formation of Al_3Zr requires some time for the nucleation events to take place, which may thus depends significantly on a cooling rate that differs according to melting pool depth. Indeed, back to eq. (ii) Souza et al. [45] showed that high cooling rate can suppress Al_3Zr phase precipitation. Shigenori Hori et al. [46] even draw the

transition between precipitation of Al_3Zr structure and α_{Al} supersatured state according to cooling rate and Zr content for Al-Zr alloys (Figure 21).

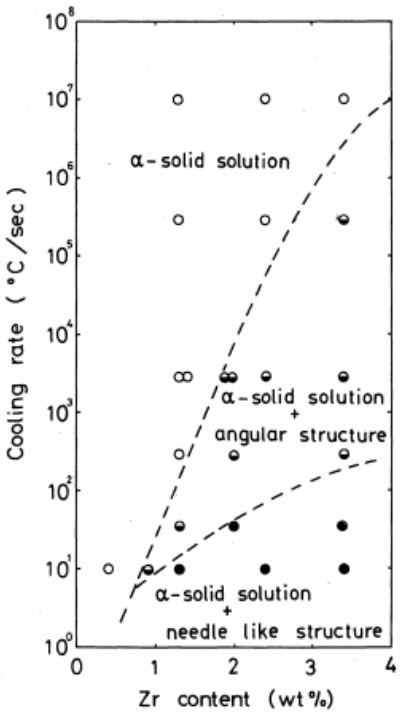

Figure 21 : Interrelations among cooling rate, zirconium content and solidified structure in Al-Zr alloys (angular structure: fine dendrite of metastable phase Al_3Zr, needle-like structure: equilibrium phase Al_3Zr) [46].

The cooling rate is expected to increase from the pool boundaries to its interior, as shown by finite elements models [32] but also analytical solutions like the Rosenthal model [47]. In this way, as Figure 21 qualitatively supports, the formation of Al_3Zr will be favoured only near the melt pool boundaries (where solidification starts): eq. (ii) occurs in equiaxed zones. In columnar regions, even though the quantity of Zr is much higher than the equilibrium maximum solid solubility of Zr in liquid aluminium [18], Zr is kept into the metastable supersatured liquid solution and Al_3Zr precipitation is prevented. On a quantitative basis, one should be careful with such a conclusion, since at typical LBM cooling rates (estimated at 10^6-10^5 K/s [48]) and with the present Zr content (roughly 1.2wt%), Figure 21 predicts the formation of the solid solution.

Nevertheless, since the current problem is dealing with nucleation mechanism, the sensitivity of the results in terms of cooling rate may be significant.

To sum things up on these matters, the resumption of columnar growth is that it should be mainly due to the nucleant site density decrease, as a result of the cooling rate increase as solidification proceeds.

4.4 Effect of added YSZ content

What is interesting to notice is that for M4%, the equiaxed bands extend towards the centre of the melt pool (Figure 22).

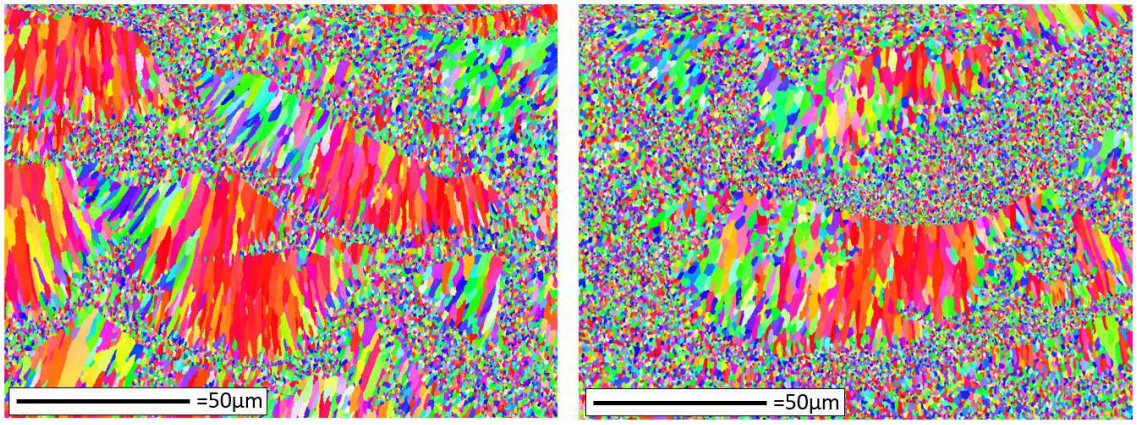

Figure 22 : EBSD IPF-Z of M2% (left) and M4% (right).

As no significant modification of the process variables are expected between M2% and M4%, such a result can be ascribed to the increase of the number of Al_3Zr seed crystals available. Indeed, as shown in Figure 20, a seed crystals density increase favours in principle the columnar to equiaxed transition. As for the underlying mechanism, one can again invoke Figure 21 showing that the necessary cooling rate for trapping Zr in solid solution increases with the Zr content in the melt, meaning that the transition cooling rate will be reached later in the solidification process.

Conclusions

Until now, almost exclusively conventional Al Alloys have been processed with the use of LBM. In this work, a new crack free 6xxx aluminium alloy was additively manufactured by LBM using mixing of pre-alloyed gas atomized Al6061 powder with an YSZ particles coating. Based on the results obtained in this study, the following conclusions can be drawn:

(1) Mixing conditions enable a good homogeneity and sturdiness regarding YSZ particles grip on aluminium powders, before, during and after the printing.

(2) Micrographs and EBSD images illustrate the effect of YSZ quantity on grain refinement. In the M1% sample, a fine equiaxed-columnar bimodal grain microstructure is observed. Cubic shaped Al_3Zr intragranular precipitates have been identified in equiaxed zones, which is a proof an undercooled region existence ahead of the solid-liquid interface. On the contrary, grains present towards the centre of the melt pools are columnar, with no intragranular Zr rich precipitates detected there. For this added quantity, not enough Al_3Zr will be able to form, meaning that the nucleation sites density is much too small to induce enough safety shields of equiaxed bands that would prevent grains from crossing one melting pool. In this respect M1% appears as a threshold value, nevertheless not high enough to fully prevent crack formation.

(3) From M2% on, the refined microstructure allows to fully accommodate the strains generated during the LBM rapid solidification process: crack free parts were observed, whatever the scanning conditions used. This particular microstructure prevents intergranular cracks to initiate and propagate.

(4) Regarding the refinement mechanism, TEM and DRX analyses support the following conclusion: YSZ particles dissolve or react in the melt under laser scanning. During cooling, and at the edges of the melt pools, Al_3Zr phases

heterogeneously precipitate on Mg/Al-oxides, and serve as nucleant for the growth of the α_{Al} equiaxed grains. Kinetic undercooling is expected to be sufficient to provide the driving force. As a result, a superfine sub-micron sized equiaxed grains band forms. Moving towards the centre of the melt pools, the higher cooling rates hinder this mechanism by limiting the Al_3Zr precipitation up to the point where columnar growth resumes. An YSZ quantity increase was seen to extend the equiaxed grain area towards the centre of the melt pool as seed crystals available increase.

Further work is necessary to assess the mechanical properties of the printed material, e.g. regarding the Al_3Zr precipitates and the grain structure effects. Another interesting perspective regarding the mechanical study of this new alloy is post heat treatment. As seen, a significant quantity of Zr is trapped into solid solution. With an appropriate ageing treatment, one can expect to precipitate nanosized Al_3Zr phases which can harden the matrix.

To sum things up, in view of the available data, this method should be transferable to other hot cracking sensitive aluminium alloys for their LBM processing. Thereby, this work can be seen as a step towards the achievement of a fully equiaxed grain structure, which would constitute a significant benefit for mechanical properties.

Acknowledgements

The authors gratefully acknowledge CEA-LITEN for financial support, Denis CAMEL, Alexis DESCHAMPS, Fernando LOMELLO, Pascal AUBRY and Nathalie PELISSIER for the constructive discussions and advice as well as Céline RIBIERE for her 3D printing

technical assistance. SERMA technologies are also thanked for the FIB lamella preparation.

References

[1] T. DebRoy *et al.*, « Additive manufacturing of metallic components – Process, structure and properties », *Prog. Mater. Sci.*, vol. 92, p. 112-224, mars 2018, doi: 10.1016/j.pmatsci.2017.10.001.

[2] N. Kang, P. Coddet, L. Dembinski, H. Liao, et C. Coddet, « Microstructure and strength analysis of eutectic Al-Si alloy in-situ manufactured using selective laser melting from elemental powder mixture », *J. Alloys Compd.*, vol. 691, p. 316-322, janv. 2017, doi: 10.1016/j.jallcom.2016.08.249.

[3] L. Thijs, K. Kempen, J.-P. Kruth, et J. Van Humbeeck, « Fine-structured aluminium products with controllable texture by selective laser melting of pre-alloyed AlSi10Mg powder », *Acta Mater.*, vol. 61, n° 5, p. 1809-1819, mars 2013, doi: 10.1016/j.actamat.2012.11.052.

[4] M. Wang, B. Song, Q. Wei, Y. Zhang, et Y. Shi, « Effects of annealing on the microstructure and mechanical properties of selective laser melted AlSi7Mg alloy », *Mater. Sci. Eng. A*, vol. 739, p. 463-472, janv. 2019.

[5] C. Weingarten, D. Buchbinder, N. Pirch, W. Meiners, K. Wissenbach, et R. Poprawe, « Formation and reduction of hydrogen porosity during selective laser melting of AlSi10Mg », *J. Mater. Process. Technol.*, vol. 221, p. 112-120, juill. 2015, doi: 10.1016/j.jmatprotec.2015.02.013.

[6] Syed Zia Uddin, « Laser powder bed fusion fabrication and characterization of crackfree aluminum alloy 6061 using in-process powder bed induction heating », présenté à Solid Freeform Fabrication Symposium – An Additive Manufacturing Conference, 2017.

[7] N. Kaufmann, M. Imran, T. M. Wischeropp, C. Emmelmann, S. Siddique, et F. Walther, « Influence of Process Parameters on the Quality of Aluminium Alloy EN AW 7075 Using Selective Laser Melting (SLM) », *Phys. Procedia*, vol. 83, p. 918-926, 2016.

[8] H. Zhao et T. Debroy, « Weld metal composition change during conduction mode laser welding of aluminum alloy 5182 », *Metall. Mater. Trans. B*, vol. 32, n° 1, p. 163-172, févr. 2001.

[9] C. M. Gourlay et A. K. Dahle, « Dilatant shear bands in solidifying metals », *Nature*, vol. 445, n° 7123, p. 70-73, janv. 2007.

[10] J. D. HUNT, « Steady state columnar and equiaxed growth of dendrites and eutectic », *Mater. Sci. Eng.*, vol. 65, n° 75-83, 1984.

[11] R. Shi, S. A. Khairallah, T. T. Roehling, T. W. Heo, J. T. McKeown, et M. J. Matthews, « Microstructural control in metal laser powder bed fusion additive manufacturing using laser beam shaping strategy », *Acta Mater.*, vol. 184, p. 284-305, févr. 2020, doi: 10.1016/j.actamat.2019.11.053.

[12] A. B. Spierings *et al.*, « Microstructural features of Sc- and Zr-modified Al-Mg alloys processed by selective laser melting », *Mater. Des.*, vol. 115, p. 52-63, févr. 2017.

[13] Q. Jia *et al.*, « Selective laser melting of a high strength Al Mn Sc alloy: Alloy design and strengthening mechanisms », *Acta Mater.*, vol. 171, p. 108-118, 2019.

[14] Q. Jia, P. Rometsch, S. Cao, K. Zhang, et X. Wu, « Towards a high strength aluminium alloy development methodology for selective laser melting », *Mater. Des.*, vol. 174, p. 107775, 2019.

[15] K. Schmidtke, F. Palm, A. Hawkins, et C. Emmelmann, « Process and Mechanical Properties: Applicability of a Scandium modified Al-alloy for Laser Additive Manufacturing », *Phys. Procedia*, vol. 12, p. 369-374, 2011.

[16] J. H. Martin, B. D. Yahata, J. M. Hundley, J. A. Mayer, T. A. Schaedler, et T. M. Pollock, « 3D printing of high-strength aluminium alloys », *Nature*, vol. 549, n° 7672, p. 365-369, sept. 2017, doi: 10.1038/nature23894.
[17] M. L. Montero-Sistiaga *et al.*, « Changing the alloy composition of Al7075 for better processability by selective laser melting », *J. Mater. Process. Technol.*, vol. 238, p. 437-445, déc. 2016.
[18] S. Griffiths, M. D. Rossell, J. Croteau, N. Q. Vo, D. C. Dunand, et C. Leinenbach, « Effect of laser rescanning on the grain microstructure of a selective laser melted Al-Mg-Zr alloy », *Mater. Charact.*, vol. 143, p. 34-42, sept. 2018, doi: 10.1016/j.matchar.2018.03.033.
[19] A. B. Spierings, K. Dawson, P. J. Uggowitzer, et K. Wegener, « Influence of SLM scan-speed on microstructure, precipitation of Al3Sc particles and mechanical properties in Sc- and Zr-modified Al-Mg alloys », *Mater. Des.*, vol. 140, p. 134-143, févr. 2018, doi: 10.1016/j.matdes.2017.11.053.
[20] M. Awd, J. Tenkamp, M. Hirtler, S. Siddique, M. Bambach, et F. Walther, « Comparison of Microstructure and Mechanical Properties of Scalmalloy® Produced by Selective Laser Melting and Laser Metal Deposition », *Materials*, vol. 11, n° 1, p. 17, déc. 2017, doi: 10.3390/ma11010017.
[21] E. A. Jägle *et al.*, « Precipitation Reactions in Age-Hardenable Alloys During Laser Additive Manufacturing », *JOM*, vol. 68, n° 3, p. 943-949, mars 2016, doi: 10.1007/s11837-015-1764-2.
[22] F. Wang, D. Qiu, Z. Liu, J. Taylor, M. Easton, et M. Zhang, « Crystallographic study of Al3Zr and Al3Nb as grain refiners for Al alloys », *Trans. Nonferrous Met. Soc. China*, vol. 24, n° 7, p. 2034-2040, juill. 2014.
[23] V. Gunenthiram *et al.*, « Experimental analysis of spatter generation and melt-pool behavior during the powder bed laser beam melting process », *J. Mater. Process. Technol.*, vol. 251, p. 376-386, janv. 2018, doi: 10.1016/j.jmatprotec.2017.08.012.
[24] C. Weingarten, D. Buchbinder, N. Pirch, W. Meiners, K. Wissenbach, et R. Poprawe, « Formation and reduction of hydrogen porosity during selective laser melting of AlSi10Mg », *J. Mater. Process. Technol.*, vol. 221, p. 112-120, juill. 2015, doi: 10.1016/j.jmatprotec.2015.02.013.
[25] A. Haboudou, P. Peyre, A. B. Vannes, et G. Peix, « Reduction of porosity content generated during Nd:YAG laser welding of A356 and AA5083 aluminium alloys », *Mater. Sci. Eng. A*, vol. 363, n° 1-2, p. 40-52, déc. 2003, doi: 10.1016/S0921-5093(03)00637-3.
[26] J. G. Kaufman et E. L. Rooy, *Aluminum alloy castings: properties, processes, and applications*. Materials Park, OH: ASM International, 2004.
[27] R. Li *et al.*, « Selective Laser Melting of Gas Atomized Al–3.02Mg–0.2Sc–0.1Zr Alloy Powder: Microstructure and Mechanical Properties », *Adv. Eng. Mater.*, vol. 21, n° 3, p. 1800650, mars 2019, doi: 10.1002/adem.201800650.
[28] *Casino, https://www.gel.usherbrooke.ca/casino/What.html*.
[29] K. Strobel, M. A. Easton, L. Sweet, M. J. Couper, et J.-F. Nie, « Relating Quench Sensitivity to Microstructure in 6000 Series Aluminium Alloys* », p. 6, 2011.
[30] LITYNSKA, « TEM and HREM study of Al3Zr precipitates in an Al-Mg-Si-Zr alloy », *J. Microsc.*, vol. 223, n° 3, 2006.
[31] A. L. Greer, A. M. Bunn, A. Tronche, P. V. Evans, et D. J. Bristow, « Modelling of inoculation of metallic melts: application to grain refinement of aluminium by Al–Ti–B », *Acta Mater.*, vol. 48, n° 11, p. 2823-2835, juin 2000.
[32] L.-E. Loh *et al.*, « Numerical investigation and an effective modelling on the Selective Laser Melting (SLM) process with aluminium alloy 6061 », *Int. J. Heat Mass Transf.*, vol. 80, p. 288-300, janv. 2015, doi: 10.1016/j.ijheatmasstransfer.2014.09.014.
[33] Y. Li et D. Gu, « Parametric analysis of thermal behavior during selective laser melting additive manufacturing of aluminum alloy powder », *Mater. Des.*, vol. 63, p. 856-867, nov. 2014, doi: 10.1016/j.matdes.2014.07.006.
[34] P. A. D. Jácome, N. V. Paraski, A. F. Ferreira, A. Garcia, et I. L. Ferreira, « EVOLUTION OF SURFACE TENSION AND GIBBS-THOMSON COEFFICIENT DURING ALUMINUM ALLOYS SOLIDIFICATION », p. 7, 2013.

[35] W. Kurz et D. J. Fisher, *Fundamentals of solidification*, 3. rev. ed., reprinted. Aedermannsdorf: Trans Tech Publ, 1992.
[36] O. Kahveci, E. Çadirli, M. Arı, H. Tecer, et M. Gündüz, « Measurement and Prediction of the Thermal and Electrical Conductivity of Al-Zr Overhead Line Conductors at Elevated Temperatures », *Mater. Res.*, vol. 22, n° 1, p. e20180513, 2019, doi: 10.1590/1980-5373-mr-2018-0513.
[37] J. Shou-Yong, L. Li-Bin, H. Ning-Kang, Z. Jin, et L. Yong, « Investigation on lattice constants of Mg-Al spinels », p. 3, 2000.
[38] J.P. Garandet, « Microsegregation in crystal growth from the melt : an analytical approach », *J Cryst. Growth*, vol. 131, p. 431-438, 1993.
[39] Y. Du *et al.*, « Diffusion coefficients of some solutes in fcc and liquid Al: critical evaluation and correlation », *Mater. Sci. Eng. A*, vol. 363, n° 1-2, p. 140-151, déc. 2003, doi: 10.1016/S0921-5093(03)00624-5.
[40] G. H. Rodway et J. D. Hunt, « Thermoelectric investigation of solidification of lead I. Pure lead », *J. Cryst. Growth*, vol. 112, n° 2-3, p. 554-562, juin 1991, doi: 10.1016/0022-0248(91)90334-2.
[41] H.A. Wilson, *Phil Mag*, vol. 50, p. 238, 1900.
[42] J. Frenkel, *Phys Z Sowjetunion*, vol. 1, p. 438, 1932.
[43] S. D. Peteves et R. Abbaschian, « Growth kinetics of solid-liquid Ga interfaces: Part II. Theoretical », *Metall. Trans. A*, vol. 22, n° 6, p. 1271-1286, juin 1991, doi: 10.1007/BF02660659.
[44] W. Tan et Y. C. Shin, « Multi-scale modeling of solidification and microstructure development in laser keyhole welding process for austenitic stainless steel », *Comput. Mater. Sci.*, vol. 98, p. 446-458, févr. 2015, doi: 10.1016/j.commatsci.2014.10.063.
[45] P. H. L. Souza, J. M. do V. Quaresma, et C. A. S. de Oliveira, « Precipitation Evolution and Modeling of Growth Kinetics of L12-structured Al3Zr Particles in Al-0.22Zr and Al-0.32Zr (wt.%) Alloys Isothermally Aged », *Mater. Res.*, vol. 20, n° 6, p. 1600-1613, août 2017, doi: 10.1590/1980-5373-mr-2017-0481.
[46] Shigenori HORI*, Shigeoki SAJI* and Akira TAKEHARA*, « Metastable phase and grain refinement in rapidly solidified Al-Zr alloys », 1981.
[47] P. Promoppatum, S.-C. Yao, P. C. Pistorius, et A. D. Rollett, « A Comprehensive Comparison of the Analytical and Numerical Prediction of the Thermal History and Solidification Microstructure of Inconel 718 Products Made by Laser Powder-Bed Fusion », *Engineering*, vol. 3, n° 5, p. 685-694, oct. 2017.
[48] P. A. Hooper, « Melt pool temperature and cooling rates in laser powder bed fusion », *Addit. Manuf.*, vol. 22, p. 548-559, août 2018, doi: 10.1016/j.addma.2018.05.032.